Magnetic and Optical Properties of Cu(II)−Bis(oxamato) Complexes: Combined Quantum Chemical Density Functional Theory and Vibrational Spectroscopy Studies

Björn Bräuer,*,†,‡ Florian Weigend,§ Federico Totti,⊥ Dietrich R. T. Zahn,† Tobias Rüffer,‡ and Georgeta Salvan†

Department of Physics and Department of Chemistry, Chemnitz University of Technology, 09107 Chemnitz, Germany, Institute for Nanotechnology, Forschungszentrum Karlsruhe, Postfach 3640, 76021 Karlsruhe, Germany, and Department of Chemistry, University of Florence, 50019 Florence, Italy

Received: December 6, 2007; In Final Form: January 25, 2008

Vibrational spectroscopies are shown to be highly sensitive to the structural modifications of paramagnetic mono- and trinuclear Cu(II)−bis(oxamato) complexes. The vibrational bands are assigned using density functional theory (DFT) calculations. Moreover, Raman spectroscopy investigations for different temperatures of thin films show that the onset of superexchange interactions at low temperatures does not involve a modification of the structural parameters. The influence of packing effects, however, on the magnetic properties is significant, as demonstrated by means of DFT using the broken symmetry approach.

Introduction

Magnetic molecules attract increasing interest due to their potential for applications such as switching layers in spintronic devices.[1] Other technological applications of magnetic molecules, for example, in magnetostrictive sensors or magneto-optical data processing units, will arise when thin films, multilayers, or nanostructures with well-defined physical properties will be produced.[2] The broad chemical variety resulting from the flexibility of carbon chemistry is of major importance for the development in this field.

Thanks to this large structural variability, Cu(II)−bis(oxamato) complexes have been used as precursors for the synthesis of multimetallic complexes (see, e.g., refs 3 and 4), building blocks for two- and three-dimensional magnetic networks,[5] and single-molecule magnets.[6,7] Their structural variability makes them also excellently suited for basic research studies of magnetic superexchange phenomena (see, e.g., refs 4 and 8−10). However, especially in the case of polymeric structures of such complexes, the structural characterization is rather difficult because in many cases no suitable crystals for single-crystal X-ray analysis are available. This limits the structural characterization of several interesting compounds in the field of molecular magnetism, like, e.g., many Co complexes. Thanks to their sensitivity to the vibrations of groups of atoms in one molecule, vibrational spectroscopies represent alternative methods in order to obtain structural information about new synthesized compounds by comparing similar complexes where, e.g., only the metals differ from each other. Furthermore, thanks to their high sensitivity to changes in the structural parameters, such as bond lengths, the temperature-dependent studies using vibrational spectroscopies can be used to monitor the correlation between the molecular structure and magnetic properties.

This work focuses on the mononuclear complexes $[M(nabo)](^nBu_4N)_2$ (M = Cu(II) (**1**) and Ni(II) (**2**)) as well as the trinuclear complexes $[Cu_3(opba)(pmdta)_2(NO_3)](NO_3)$ (**3**) and $[Cu_3(nabo)(pmdta)_2(BF_4)](BF_4)$ (**4**) where opba = *o*-phenylene-bis(oxamato), nabo = 2,3-naphthalene-bis(oxamato), and pmdta = *N*,*N*,*N*′,*N*″,*N*″-pentamethyldiethylenetriamine. The Lewis formulas of the investigated complexes are shown in Figure 1. They consist of the entities $[Cu(nabo)]^{2-}$, $[Ni(nabo)]^{2-}$, $[M(opba)]^{2-}$, and $[Cu(pmdta)]^{2+}$. The synthesis of compound **4** including a naphthyl instead of a phenyl unit (cf., **3**) as central N,N′-bridge was performed in order to improve the optical properties by increasing the absorption intensity using a more extended aromatic system compared to that of **3**. Strong absorbing properties are important prerequisites, e.g., for obtaining highly effective magneto-optical media.

Recently, spin coating[11] was used to prepare films of several nanometers thickness for materials which are not sublimable, such as bis(oxamato) Cu complexes. This method allows a good control of the film thickness while preserving the molecular structure, as proven by means of Raman spectroscopy (RS).

In this work the optical and vibrational properties of the complexes **1**−**4** are characterized by means of UV−vis, ellipsometry, infrared, and Raman spectroscopic measurements of solution, powders, and thin films. The assignment of the vibrational modes is sustained by theoretical calculations with density functional theory (DFT) methods. The theoretical calculations are further employed to demonstrate the influence of structural deformations induced by packing effects in the crystalline state and charging effects induced by counterions on the superexchange interactions between the Cu centers within the trinuclear complexes.

Experimental and Computational Procedures

Syntheses and Crystal Structure Analysis. The complexes **1**, **2**, **3**, and **4** were produced using published procedures.[9,12] Approximately 300 nm thick films of organic molecules were prepared by means of spin coating. For this purpose a saturated acetonitrile solution of the respective compounds was prepared and spin-coated (100 rounds per min rotation speed) on a silicon substrate covered with natural SiO_2.

The crystal structures of compound **1**, **2**, and **3** were determined by Rüffer et al.[9] The crystal structures of **1** and **2**

* Corresponding author. E-mail: bbj@hrz.tu-chemnitz.de.
† Department of Physics, Chemnitz University of Technology.
‡ Department of Chemistry, Chemnitz University of Technology.
§ Forschungszentrum Karlsruhe.
⊥ University of Florence.

10.1021/jp711506t CCC: $40.75
Published on Web 04/15/2008

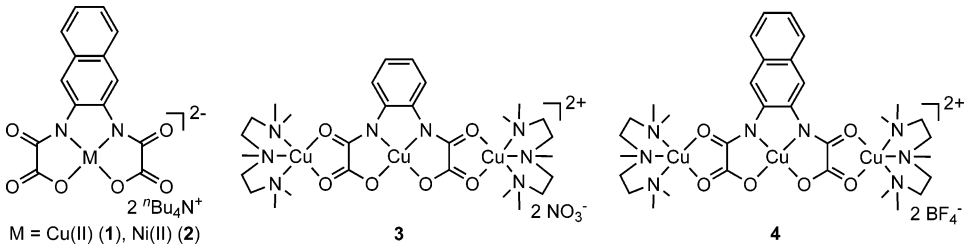

Figure 1. Lewis formulas of the compounds under investigation.

consist of discrete $[^nBu_4N]^+$ cations and $[M(dana)]^{2-}$ anions, respectively, and crystallize in the monoclinic space group *C*2/*c* with four formula units in the unit cell. The anionic entities possess crystallographically imposed C_2 symmetry and have an almost planar structure with maximum deviations from the mean molecular planes of 0.054(2) Å.

The structure of **3** consists of cationic trinuclear entities $[Cu_3(opba)(pmdta)_2(NO_3)]^+$ and a noncoordinated nitrate anion molecule. The structure of **4** consists of a cationic trinuclear entity $[Cu_3(nabo)(pmdta)_2(BF_4)]^+$ and a noncoordinated tetrafluoroborate anion. **3** crystallizes in the monoclinic space group *P*2(1)/*n*, and **4** crystallizes in *P*2(1)/*c* with four formula units in the unit cell. The cationic entities possess crystallographically imposed C_1 symmetry.

Raman Spectroscopy. A He-cooled cryostat attached to a Raman spectrometer allows temperature-dependent measurements in the range from 15 to 300 K to be performed. The spectra presented in this work were recorded in a macroconfiguration at 15 K unless specified otherwise. The Raman spectra were excited with the 21 839 cm^{-1} (457.9 nm) line of an Ar^+ laser and with the 15 454 cm^{-1} (647.1 nm) line of a Kr^+ laser. The 647.1 nm line lies in the lower energy tail of the HOMO−LUMO optical transition of all compounds, whereas the 457.9 nm line is located at the onset of the next higher energy optical transition. The scattered light is collected by a Dilor XY 800 triple monochromator with a multichannel charge-coupled device detector. The spectral resolution was ∼4 cm^{-1} as determined from the full width at half-maximum (fwhm) of the laser line. Typical values of the incident laser power were in the range from 5 to 10 mW. The polarization of the scattered light was not analyzed in this work.

Infrared Spectroscopy. The IR spectroscopy measurements of complexes embedded in KBr pellets were performed at room temperature with a resolution of 2 cm^{-1} using a Perkin-Elmer infrared spectrometer "Spektrum 1000".

Absorption Spectroscopy. Absorption measurements in solution were performed using 10^{-5} M and 10^{-3} M CH_3CN solutions. The spectra were measured in the range from 11 000 to 42 000 cm^{-1} at room temperature using a Thermo Spectronics UV−vis spectrometer "Genesys 6".

Spectroscopic Ellipsometry. Variable-angle spectroscopic ellipsometry (VASE) measurements were performed in the energy range of 1.0−5.0 eV with a step width of 0.02 eV and angles of incidence of 68°, 71°, and 74° using a Woollam VASE ellipsometer. Ellipsometry measures the quantities ψ and Δ which are related to the ratio of the effective Fresnel coefficients *r* for s- and p-polarized light by the expression $r_p/r_s = \tan \Psi \exp(i\Delta)$.

Density Functional Theory Calculations of Vibrational Frequencies. Calculation of vibrational spectra as well as previous optimization of structure parameters was carried out for **1**−**3** at DFT level with the B3LYP hybrid functional.[13,14] The counterions were neglected, leading to the dianionic species $[M(opba)]^{2-}$ (M = Cu(II) (**1′**) and Ni(II) (**2′**)) and the dicationic species $[Cu_3(opba)(pmdta)_2]^{2+}$ (**3′**). **1′** and **2′** were treated with the program package Gaussian 03[15] employing 6-311G basis sets; **3′** was calculated with TURBOMOLE[16] taking advantage of the RI-J approximation[17] using def2-TZVP[18] basis sets and corresponding auxiliary basis sets.[19] For charged molecules it seems reasonable to compensate the excess charge, e.g., with a conductor-like screening model (COSMO),[20] i.e., by placing the molecule in a cavity defined by the molecular shape, and to impose a constant electrostatic potential on the cavity surface. This was done for the calculation of magnetic exchange parameters, see below, but not for the calculation of vibrational frequencies, as calculation of these quantities within the COSMO model is not implemented in TURBOMOLE for conceptual reasons (a vibrational mode would change the shape of the cavity which is not accounted for, as frequencies are calculated from the second derivatives of the energy for a fixed geometric structure). As effects of COSMO on vibrational frequencies are expected to be small, the calculation of frequencies without the COSMO model is sufficient to allow for an assignment of the modes.

Calculation of Magnetic Superexchange Parameters. The broken symmetry (BS) approach developed by Noodleman[21,22] was used to calculate the coupling parameters for the magnetic superexchange. The BS determinant is built from spin orbitals localized on two spin centers. Therefore, the magnetic properties of insulating molecular magnetic materials are investigated by partitioning the magnetic interaction in spin−spin interaction of pairs of paramagnetic centers on which the unpaired electrons are localized leading to a spin Hamiltonian of the type

$$H = -\sum_{i<j} J_{ij}\mathbf{S}_i\cdot\mathbf{S}_j = -J_{12}(\mathbf{S}_{cu1}\cdot\mathbf{S}_{cu2}) - J_{12'}(\mathbf{S}_{cu1}\cdot\mathbf{S}_{cu2'}) - J_{22'}(\mathbf{S}_{cu2}\cdot\mathbf{S}_{cu2'}) \quad (1)$$

where $\mathbf{S}_{Cu}$ are the spins associated with the different paramagnetic Cu centers with Cu1 in the middle and Cu2/Cu2′ in the terminal positions of the complex. J_{ij} are the respective isotropic magnetic exchange coupling constants. The following eigenvalues *E* result from the four eigenstates $|(\mathbf{S}_{cu2})(\mathbf{S}_{cu1})(\mathbf{S}_{cu2'})\rangle$:

$$\text{HS:}\quad M\text{s} = \pm 3/2 \quad \text{and} \quad |(1/2)(1/2)(1/2)\rangle \rightarrow E_{HS} = -\frac{J_{12}}{4} - \frac{J_{12'}}{4} - \frac{J_{22'}}{4}$$

$$\text{LS1:}\quad M\text{s} = \pm 1/2 \quad \text{and} \quad |(1/2)\overline{(1/2)}(1/2)\rangle \rightarrow E_{LS1} = +\frac{J_{12}}{4} + \frac{J_{12'}}{4} - \frac{J_{22'}}{4}$$

$$\text{LS2:}\quad M\text{s} = \pm 1/2 \quad \text{and} \quad |\overline{(1/2)}(1/2)(1/2)\rangle \rightarrow E_{LS2} = +\frac{J_{12}}{4} - \frac{J_{12'}}{4} + \frac{J_{22'}}{4}$$

$$\text{LS2}'\text{:}\quad M\text{s} = \pm 1/2 \quad \text{and} \quad |(1/2)(1/2)\overline{(1/2)}\rangle \rightarrow E_{LS2'} = -\frac{J_{12}}{4} + \frac{J_{12'}}{4} + \frac{J_{22'}}{4} \quad (2)$$

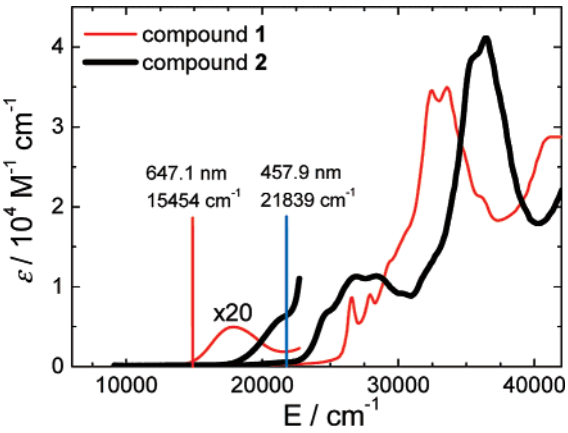

Figure 2. Absorption spectrum of **1** and **2**. The laser lines for the Raman investigations are shown as vertical lines.

where HS means high spin with three parallel oriented spins and LS stands for the remaining low-spin configurations. In order to determine the *J* parameters the total energy of each spin configuration is calculated. The respective energy differences provide the values of *J*, according to eq 2.

This approach is often used in order to obtain a meaningful set of exchange coupling parameters in systems with several different coupling parameters.[23] However, the quantitative accuracy of the current DFT approaches for transition metal complexes is not always satisfactory. Numerous functionals were investigated for several transition metal complexes as well as for main group radicals[24] and were shown not to improve substantially the accuracy of the popular B3LYP functional. This method is also most consistent with total energy calculations, and thus it is the method of choice for the following calculations.

In the present case, single-point energies were calculated for the experimental structures obtained from single-crystal X-ray crystallography[9] for $[Cu_3(opba)(pmdta)_2]^{2+}$ (**3′**), $[Cu_3(nabo)(pmdta)_2]^{2+}$ (**4′**), $[Cu_3(opba)(pmdta)_2(NO_3)]^{+}$ (**3′** NO_3^-), $[Cu_3(nabo)(pmdta)_2(BF_4)]^{+}$ (**4′** BF_4^-) using TURBOMOLE, as noted above with and without the COSMO model.

Results and Discussions

UV−Vis and Spectroscopic Ellipsometry Studies. The absorption spectra of **1** and **2** from measurements in CH_3CN solution are shown in Figure 2. In the visible range weak d−d transitions appear at 17 800 cm^{-1} (ϵ = 250 M^{-1} cm^{-1}) for **1** and 21 600 cm^{-1} (ϵ = 320 M^{-1} cm^{-1}) for **2**. This difference in the energy position is due to the different electronic ground state configurations of Cu(II) with $[Ar]3d^9$ and Ni(II) with $[Ar]3d^8$. For energies above 20 000 cm^{-1} charge transfer and $\pi-\pi^*$ transitions are observed. The differences in the line shape and the energetical position of the bands is due to different coordination behavior of Cu(II) and Ni(II). The former transition metal ion coordinates much stronger than the latter.

The absorption spectra of **3** and **4** from measurements in solution are shown in Figure 3 (left). The ϵ_2 plots obtained from VASE measurements are shown in Figure 3 (right). VASE delivers valuable information concerning the absorption behavior of the molecules on the substrate. The dielectric function in the range from 0.8 to 5 eV was evaluated considering the layers as isotropic. In a first step a point-by-point fit of the measured ellipsometric angles Ψ and Δ was performed, i.e., fitting the calculated ellipsometric parameters to the experimental data at each wavelength separately, cf., Figure a1 of the Supporting Information for **4** and ref 11 for **3**. In the next step a sum of Gaussian oscillators was used to simulate the line shape of the imaginary part of the dielectric function ϵ_2, while the real part of the dielectric function ϵ_1 is generated according to the Kramers−Kronig relation. The spectral behavior of ϵ_1, Ψ, and Δ is given in Figures a1 and a2 in the Supporting Information.

At energies of 16 800 cm^{-1} (ϵ = 1300 M^{-1} cm^{-1}) for **3** and 17 000 cm^{-1} (ϵ = 1400 M^{-1} cm^{-1}) for **4** d−d and charge transfer transitions of the Cu(II) ions appear, and above 20 000 cm^{-1} charge transfer and $\pi-\pi^*$ transitions dominate the spectrum. The latter are more intensive for **4** due to the enlarged aromatic system in comparison to **3**. This trend is clearly observable also in the line shape of ϵ_2 of films determined from VASE investigations. In contrast, the transitions at lower energy show almost the same intensity and are only slightly shifted to higher wavenumbers for **4**.

IR and Raman Spectra for 1 and 2. The experimental and calculated IR and Raman spectra of **1** and **2** are shown in Figures 4 and 5, and the proposed mode assignment is presented in Table 1. The calculated spectra were obtained by broadening the calculated vibrational lines with Lorentz functions having a fwhm of 5 cm^{-1}, value that corresponds to the typical fwhm of the bands in the experimental spectra. Due to the low symmetry of the molecule, the same modes are both Raman- and IR-active.

At a first glance the comparison between the experimental and the calculated IR spectra shows some differences concerning the number of modes exhibiting significant intensity. The additional modes observed in the experimental spectra can be attributed to the $^nBu_4N^+$ counterion which was neglected in the calculations. In contrast, the calculated Raman spectra fit much better to the experimental data. $^nBu_4N^+$ is a noncoordinating counterion due to steric reasons. Thus, a charge transfer from the $[Cu(nabo)]^{2-}$ (**1′**) entity to $^nBu_4N^+$ is not possible, and the energy of its first optical transition lies well above the excitation energy used in this work. Therefore, its Raman-active bands cannot be resonantly enhanced by the excitation energy used and should have a Raman cross section much smaller compared to that of **1**.

For the assignment of the experimental modes to elongations of atom groups within the molecules, the comparison between the experimental vibrational spectra of the Cu (**1**) and the corresponding Ni (**2**) complex with the theoretically predicted spectra was taken into consideration. The root-mean-square (rms) deviation of the calculated from the measured IR frequencies is 20 cm^{-1} for **1** and 23 cm^{-1} for **2**. This rms value could be mainly due to the fact that the IR-active counterion $^nBu_4N^+$ was neglected in the theoretical calculations.

In the case of the Raman investigations the rms deviation is 6 cm^{-1} for **1** and 10 cm^{-1} for **2** The low rms deviations indicate a very good agreement between the calculations and the experimental spectra. The correlation between the calculated and the measured wavenumbers is shown in Figure 6, parts a and b. The red line represents the best fit in the range of 500−3300 cm^{-1} with a slope of 1.06 and 1.09 for **1** and **2**, respectively. As expected,[25] the hybrid-DFT methods slightly overestimate vibrational frequencies.

The blue line represents the best fit in the range of 500−1700 cm^{-1}. The slope of the blue line is 1.00 for **1** and 0.97 for **2** which clearly indicates that the mismatch between the experimental and calculated frequencies strongly depends on which vibrational modes were excited. It should be noted that no clear trend for the mismatch value and size with increasing frequency was observed. That is why the calculated spectra were not shifted here in contrast to the investigations on complex **3**, see below.

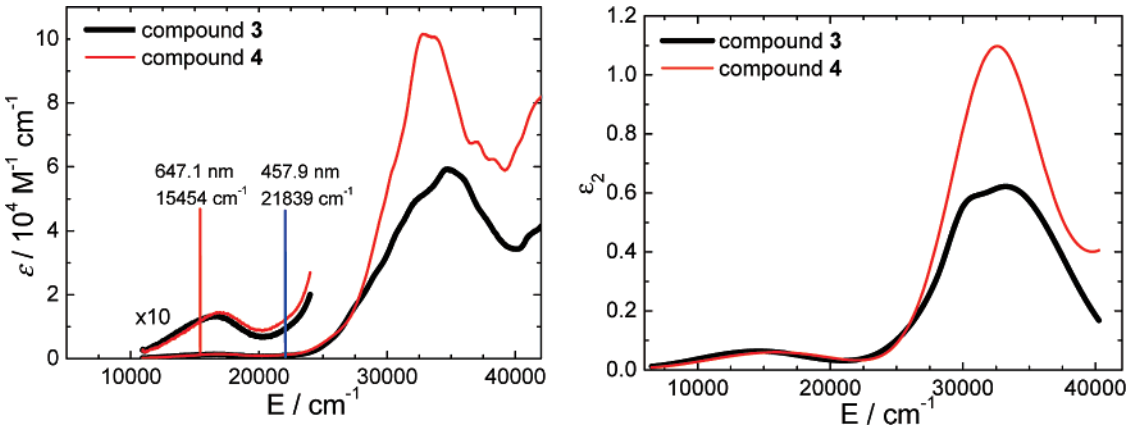

Figure 3. Absorption spectrum of **3** and **4** (left) in comparison with the respective imaginary part of the dielectric function (right). The energy positions of the laser lines used for the Raman investigations are shown by vertical lines (left).

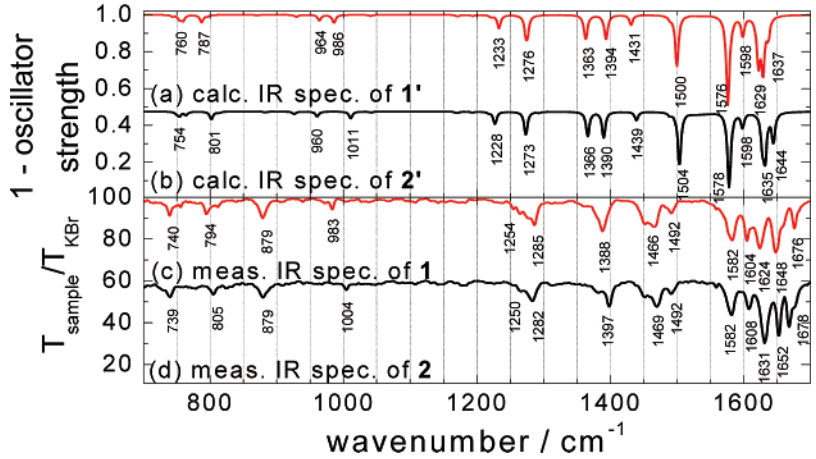

Figure 4. Comparison of the calculated IR spectra of **1′** (a) and **2′** (b), which correspond to **1** and **2** when neglecting the counterions, and the measured IR spectra of **1** (c) and **2** (d). The calculated oscillator strengths were divided by 2000. For clarity the spectra c and d were vertically shifted.

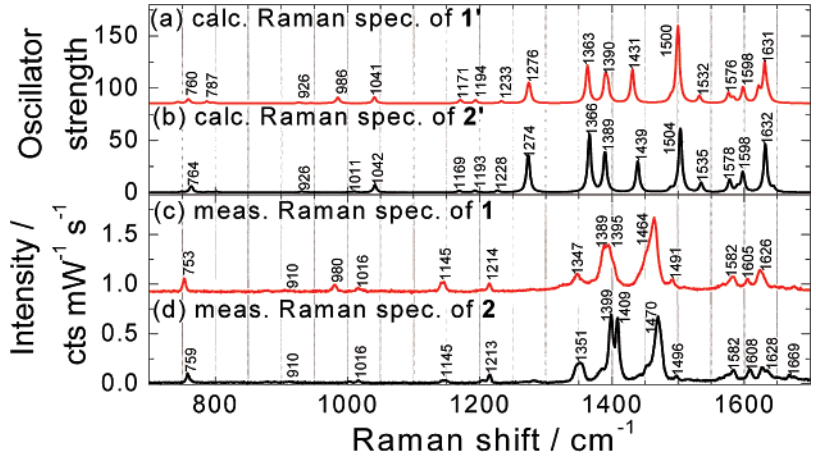

Figure 5. Comparison of the calculated Raman spectra of **1′** (a) and **2′** (b), which correspond to **1** and **2** when neglecting the counterions, and the measured Raman spectra of **1** (c) and **2** (d). For clarity the spectra c and d were vertically shifted.

Both techniques, IR and Raman spectroscopies, are very sensitive to the coordination of the transition metal ion. The Cu(II) ion is stronger coordinated to nitrogen than the Ni(II) ion[9] leading to a lower electron density[10] in the ligand system of **1**. Thus most of the vibrational modes of the ligand should appear at lower frequencies in the case of **1** compared to **2**. This fact provides an experimental criterion that can be used to support the assignment of the mode characters. Indeed, the breathing modes of the aromatic system appear in the IR spectrum at 545 cm^{-1} (calcd 555 cm^{-1}) and 549 cm^{-1} (calcd 568 cm^{-1}) for **1** and **2**, respectively. Even though localized on the O−M−N skeleton, the change in the electron density when replacing the metal atom (M) also extends over the central bridge, in this case the naphthyl group. Therefore, also the ring vibrations ν(CC) are influenced by the difference in the electron density, but to a lesser extent, cf., 1464 cm^{-1} (calcd 1500 cm^{-1}) and 1470 cm^{-1} (calcd 1504 cm^{-1}) for **1** and **2**, respectively. For the CO stretching vibrations the same systematic tendency

TABLE 1: Assignment of Infrared (IR) and Raman (R) (λ = 457 nm, T = 15 K) Spectra of 1 and 2[a,b]

		spectroscopic data of **1**				spectroscopic data of **2**			
		IR investigations		R investigations		IR investigations		R investigations	
mode	symmetry	calcd	measd	calcd	measd	calcd	measd	calcd	measd
δ(CO), δ(MO), δ(MN)	B_2	360 w		360 vw				360 vw	
δ(CC oop)	B_1	364 w						370 vw	
δ(OMN), δ(ring^1 rotation)	B_2	374 w							
δ(OMN), δ(CC) of ring^{1,2}	B_1					441 w			
δ_{sym}(CC oop)	B_1	461 w				453 w			
δ_{sym}(CC, CH oop)	B_1	498 m				496 m			
δ_{asym}(CC) of ring^{1,2}, ν_{asym}(MN)	B_2	554 w				564 w			
δ_{sym}(ring^{1,2} breathing)	A_1	555 w				568 w	549 w		
δ_{sym}(CC, CH, CN oop)	B_1	576 w	558 w			568 w			
δ_{sym}(ring^{1,2} breathing)	A_1			581 vw					
δ_{asym}(CC) of ring^{1,2}, δ(OCuC), δ(NCC)	B_2	587 vw				593 vw	563 vw		
δ(ring^{1,2}), δ(OCO)	B_2	744 vw				750 vw			
δ_{sym}(CH oop)	B_1	754 w				754 w			
δ_{asym}(CC, CH)	A_1	760 w	740 w	760 w	753 m	764 w	739 w	764 w	759 m
δ_{sym}(OCO, NCO oop)	B_1							790 vw	
δ_{sym}(OCO), δ_{sym}(ring^{1,2} breathing)	A_1	787 w	794 w			801 w	805 w		
ν_{sym}(CC)	A_1	870 vw	879 m			883 vw	879 m		
δ_{asym}(ring^{1,2})	B_2			926 vw	910 vw			926 vw	910 w
δ_{sym}(CH oop)	B_1	929 vw				926 w			
δ_{sym}(CH oop)	B_1	964 w				960 w			
δ_{asym}(CNC), δ_{asym}(CH)	B_2							1003 vw	
ν_{sym}(MN), δ_{sym}(CH)	A_1	986 w	983 w	986 w	980 w	1011 w	1004 w	1011 w	
δ_{sym}(CH), δ_{sym}(ring^2 breathing)	A_1	1041 vw		1041w	1016 w	1042 vw		1042 w	1016 w
δ_{sym}(CH), δ_{sym}(ring^1 breathing) ν_{sym}(CNC)	A_1	1171 vw		1171 vw	1145 w	1169 vw		1169 vw	1145 w
δ_{sym}(CH)	A_1	1194 vw		1194 vw		1193 vw		1193 vw	
δ_{asym}(CH), ν_{asym}(CO)	B_2	1221 vw				1218 vw			
δ_{sym}(CH), ν_{sym}(CO)	A_1	1233 w	1254 w	1233 vw	1214 w	1228 m	1250 w	1228 vw	1213 w
ν_{asym}(CC), δ_{asym}(CH), δ_{asym}(CC) of ring^{1,2}	B_2	1276 m	1285 m	1276 m		1273 m	1282 m	1273 m	
δ_{sym}(CH), δ_{sym}(ring^1 breathing), ν_{sym}(CC)	B_2	1274 m		1274 w	1347 m	1274 m		1274 s	1351 m
δ_{asym}(CH), δ_{asym}(ring^{1,2})	B_2	1360 w	1366 w	1360 w		1366 w	1382 w	1366 w	
ν_{sym}(CC, CC) of ring^{1,2}, δ_{sym}(CH), ν_{sym}(CN)	A_1	1363 m		1363 m	1389 s	1366 s		1366 s	1399 s
ν_{sym}(CC, CC) of ring^{1,2}, ν_{sym}(CN), δ(NCuN scissoring)	A_1	1390 vw		1390 m	1395 s	1389 vw		1389 s	1409 s
δ(NCuN rocking), δ_{asym}(CH) of ring^2	B_2	1394 m	1388 m	1394 m		1390 m	1397 m	1397 m	
δ_{sym}(CH), ν_{sym}(CC) of ring^{1,2}	A_1	1431 w	1466 m	1431 m		1439 w	1469 m	1439 m	
δ_{asym}(CH), δ_{asym}(ring^{1,2}), ν_{sym}(CN)	B_2	1489 w		1489 w		1489 w		1489 w	
δ_{sym}(CH), ν_{sym}(CC) of ring^1	A_1	1500 s	1492 w	1500 s	1464 vs	1504 s	1492 w	1504 s	1470 vs
δ_{sym}(CH), ν_{sym}(CC) of ring^2	A_1	1532 vw		1532 w	1491 w	1535 w		1535 w	1496 w
δ_{asym}(CH), ν_{sym}(CO), ν_{asym}(ring^1)	B_2	1576 vs	1582 s	1576 w	1582 m	1578 vs	1582 m	1578 w	1582 m
ν_{sym}(CO), ν_{sym}(CC) of ring^{1,2}	A_1	1584 w		1584 w				1590 w	
ν_{sym}(CO), ν_{sym}(CC) of ring^{1,2}	A_1	1598 w	1604 m	1598 m	1605 w	1598 w	1608 m	1598 m	1608 m
ν_{asym}(CO, CC) of ring^{1,2}	B_2	1622 s	1624 s	1622 m		1628 s	1631 s		
ν_{asym}(CO, CC) of ring^{1,2}	B_2	1629 s				1632 s		1632 s	1628 m
ν_{asym}(CO, CC) of ring^{1,2}	B_2	1631 vw	1648 s	1631 m	1626 m	1635 s	1652 s	1635 m	1629 m
ν_{sym}(OCO)	A_1	1637 m	1676 m	1637 w	1657 vw	1644 m	1678 s	1644 w	1669 w
ν_{asym}(CH) of ring^2	B_2			3114 w				3115 w	
ν_{sym}(CH) of ring^2	A_1	3129 w	2873 m	3129 m		3130 w	2874 m	3130 m	
ν_{asym}(CH) of ring^2	B_2	3145 m	2930 m	3145 m		3145 m	2932 m	3145 m	
ν_{sym}(CH) of ring^2	A_1	3158 m	2961 m	3158 s		3159 m	2962 m	3159 s	
ν_{sym}(CH) of ring^1	A_1			3204 m				3208 m	

[a] Assignment: oop, out-of-plane vibration; ν, stretching vibration; δ, deformation vibration; ring^1, nitrogen-substituted aromatic naphthyl ring; ring^2, remaining aromatic naphthyl ring. [b] Frequencies are given in cm^{-1}; v, very; w, weak; m, medium; s, strong.

was observed, cf., e.g., 1648 cm^{-1} (calcd 1631 cm^{-1}) and 1652 cm^{-1} (calcd 1635 cm^{-1}) for **1** and **2**, respectively. For a schematic visualization of the elongation patterns of some selected modes see Figure 7.

Further support for the mode assignment was gained by an inspection of the relative intensities in the IR and Raman spectrum. The most intensive bands in the Raman spectrum are expected to be the CH deformation vibrations, whereas in the IR spectrum the stretching vibrations of CO should dominate. Representative for the former are the modes at 1389 cm^{-1} (calcd 1363 cm^{-1}) and 1464 cm^{-1} (calcd 1500 cm^{-1}) for **1** and those at 1399 cm^{-1} (calcd 1366 cm^{-1}) and 1470 cm^{-1} (calcd 1504 cm^{-1}) for **2**. Exemplary CO modes are located at 1582 cm^{-1} (calcd 1576 cm^{-1}) for **1** and 1582 cm^{-1} (calcd 1578 cm^{-1}) for **2.**

Experimental IR and Raman Spectra and Their Assignment for Complex 3. The optimized molecular structure of **3** is shown in Figure 8. The measured IR as well as the calculated IR and Raman spectra of **3** are shown in Figure 9, and the mode assignment based on the comparison between the experimental and calculated spectra is provided in Table 2. Because of the low symmetry of the molecule, the same modes are both Raman-

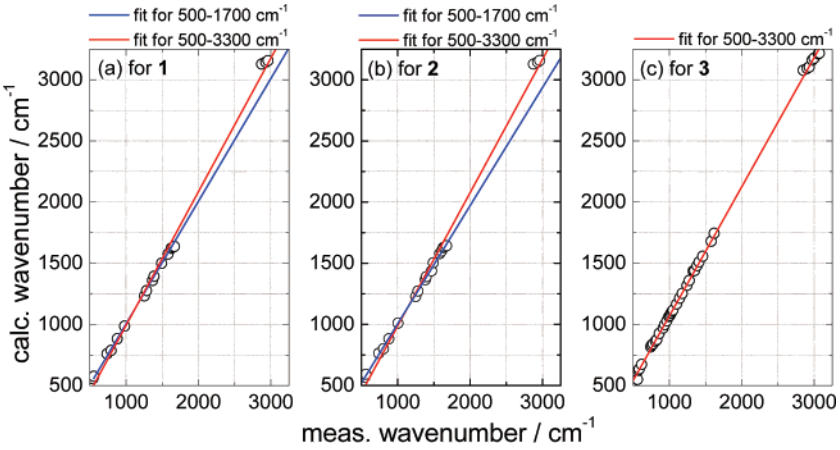

Figure 6. Correlation of calculated and measured IR wavenumbers for **1**, **2**, and **3**.

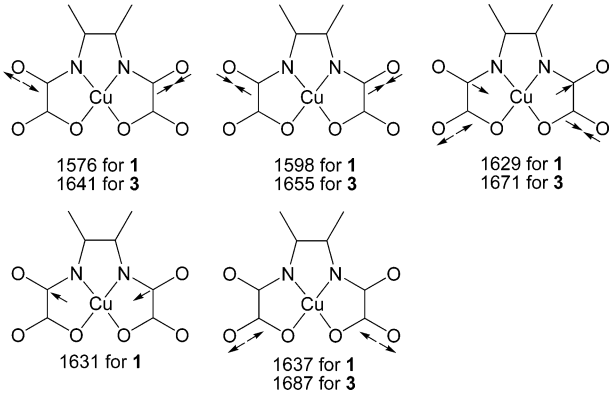

Figure 7. Elongation patterns of the CO stretching vibrations of compounds **1** and **3** with their calculated frequencies.

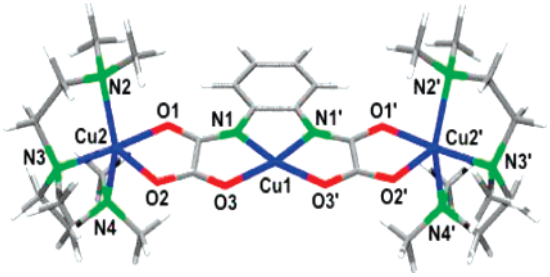

Figure 8. DFT-optimized structure of **3**.

and IR-active. The frequencies of the calculated spectrum were multiplied by a factor of 1.06 to get a better match to the experimental frequencies (cf., Figure 6). To recall, in general DFT methods slightly overestimate vibrational frequencies.[25] After this procedure the calculated and measured IR spectra show very good agreement which is underlined by the small rms deviation of 5 cm^{-1}. The fact that a multiplication by a factor improves the correspondence between the calculated and experimental spectra for **3**, but it would less improve it for the complexes **1** and **2**, is due to the larger rms deviation for **1** and **2** in comparison to **3**. The reasons for such differences are not clear at this point; they could, for instance, arise from slight structural differences of the complex in the solid state and after the geometry optimization or because of neglecting the counterions resulting in the dianionic species $[M(opba)]^{2-}$ (M = Cu(II) (**1′**) and Ni(II) (**2′**)) and the dicationic species $[Cu_3(opba)(pmdta)_2]^{2+}$ (**3′**), respectively.

The spectra of **3** are dominated by the vibrational modes of the aromatic and the terminal pmdta ligand system, cf., deformation vibrations in the range of 1000−1600 cm^{-1} and

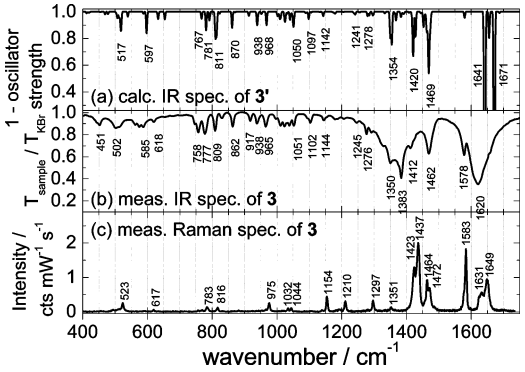

Figure 9. Comparison of the calculated IR spectrum of **3′** (a) which corresponds to **3** neglecting the counterions, the measured IR spectrum of **3** (b) on a KBr pellet, and the measured Raman spectrum of **3** (c) on a 300 nm thick film on Si/SiO_2.

stretching vibrations at 2894 − 3090 cm^{-1}. In the range of 1600−1700 cm^{-1} the stretching vibrations of CO and CN bonds appear. The fwhm of the IR bands around 1400 and 1600 cm^{-1} is larger compared to the bands in the same region of the mononuclear complexes. This broadening effect was also observed for other trinuclear Cu(II)−bis(oxamato) complexes, not shown here, and is most probably due to the asymmetry of the complexes in the solid state where the terminal pmdta ligand systems induce slightly different binding angles with Cu(II) and thus differences in the charge density distribution in the right and the left oxamato groups.

Furthermore, the broadening of the IR bands is higher in comparison with the Raman bands. This observation can be explained taking into account the presence of the solvent molecules that are embedded between the transition metal complexes during the crystallization procedure from solution. The solvent molecules show almost no absorption in the visible spectral range, and thus no high Raman intensities are expected, whereas in IR their vibrations can be excited, leading to the observed broadening effects. The smaller number of bands in the DFT calculation is a consequence of the higher symmetry achieved during structure optimization, as symmetry-breaking counterions are neglected.

As for the mononuclear complexes, the relative intensities can be again used to cross-check the band assignment. The largest intensities are observed for the δ(CH) modes at 1437 and 1583 cm^{-1} in the Raman spectrum, whereas in IR the ν(CO) are the most intensive bands, cf., 1620 cm^{-1} (calcd 1641, 1671 cm^{-1}).

The excitations of the Raman scattering process were also performed using the red light of a krypton laser (1.92 eV, 647

TABLE 2: Assignment of Infrared (IR) and Raman (R) (λ = 457 nm, T = 15 K) Spectra of 3[a,b]

mode	calcd IR	measd IR	measd R
ν(CuN3), δ(CH_3)	411 vw		
ν(CuN2, CuN4)	418 vw		
δ(CH_3), δ(COCu), δ(CH ring)	468 vw	451 w	
ν(CuN2, CuN3, CuN4)	477 w		
ν(CuN2, CuN4)	506 w	502 w	
ν(CuN3), ν(CuO1)	517 m	562 w	
δ(CC ring oop)	538 w		523 w
δ(CNC) of pmdta	587 vw	562, 574 w	
δ(Cu1O, Cu1N)	597 m	585 w	
δ(CC ring)	632 w	618 vw	617 vw
δ(CC oop), δ(CH ring oop)	653 w		
ν(CuN2, CuN3, CuN4)	767 w	744 w	
ν(CuN2, CuN4)	781 m	758 m	
δ(CC ring), ν(OCu1O), δ(NCu1N), ν(Cu2O, Cu2′O)	791 w	777 m	783 w
ν(CuN) of pmdta	811 m	809 m	816 w
ν(O2CO2), ν(O1CN1), δ(CC ring)	822 vw	829 w	
δ(CC oop)	870 m	862 m	
ν(CC) of pmdta	913 vw	917 w	
δ(CH_2) rocking of pmdta, ν(NCH_3) of pmdta	938 w	938 w	
δ(CH_2) rocking of pmdta, ν(NCH_3) of pmdta	968 w	965 m	975 w
ν(NCH_3) of pmdta	1001 w	996 w	
δ(CH), δ(NCu2N, NCu2′N), ν(NCH_3) of pmdta	1009 w	1011 w	
δ(CH_2) rocking of pmdta	1025 w	1023 w	1032 vw
δ(CH_2) rocking of pmdta	1040 w	1038 w	1044 vw
δ(CH_2) twisting of pmdta	1050 m	1051 w	
δ(CH_2) twisting of pmdta	1097 w	1102 w	
δ(CH_2) twisting of pmdta	1142 vw	1144 w	1154 m
δ(CC ring)	1178 vw	1179 vw	
δ(CH_2) twisting of pmdta	1241 vw	1245 vw	1210 w
δ(CH ring)	1278 w	1276 w	1297 w
δ(CH_2) twisting of pmdta	1285 w		
δ(CH_2) twisting of pmdta	1295 w		
δ(CH_2) wagging of pmdta	1332 vw		
δ(CH_2) wagging of pmdta	1350 m	1330 s	
ν(CC)	1354 s	1350 s	1351 vw
ν(CC)	1368 w		
δ(CH_3) scissoring	1383 w		
δ(CH_3) scissoring	1391 w	1383 s	
δ(CH_3) scissoring	1420 s	1412 m	1418 s
δ(NCuN, OCuO), ν(CC) of ring and oxamato group	1428 m		1423 s
δ(aliph CH)	1452 w		1437 vs
δ(aliph CH)	1463 m	1462 s	1464 s
δ(aliph CH)	1469 s		1472 m
δ(arom CH)	1579 w	1578 m	1583 vs
ν(CO), ν(CN) asym	1641 vs	1620 vs	1631 m
ν(CO), ν(CN) sym	1655 m		1649 s
ν(CO), ν(CN) asym	1671 vs		
ν(CO), ν(CN) sym	1687 w		
ν(aliph CH)	2894 m	2807, 2849 w	
ν(aliph CH)	2909 w	2883, 2903 m	
ν(aliph CH)	2919 m	2931 m	
ν(aliph CH)	2973 vw	2975 m	
ν(aliph CH)	2987 m	3000 m	
ν(aliph CH)	3019 w	3058 w	
ν(aliph CH)	3026 w	3073 w	
ν(arom CH)	3055 vw		
ν(arom CH)	3065 vw		
ν(arom CH)	3090 vw		

[a] Assignment: oop, out-of-plane vibration; ν, stretching vibration; δ, deformation vibration; atom labels refer to the atom numbering scheme in Figure 8. [b] Frequencies are given in cm^{-1}; v, very; w, weak; m, medium; s, strong.

nm). Even though its energy is located in the lower energy tail of the HOMO−LUMO absorption band, cf., Figure 3, the intensity of the Raman bands excited using the 647 nm line is 2 orders of magnitude lower in comparison to the excitation using the 457 nm line. Recalling that the 647.1 nm line is located at the onset of the d−d transition, whereas the 457.9 nm is at the onset of the next higher energy transition, the low Raman cross section for the 647.1 compared to the 457.9 nm excitation line is an additional indication that the lowest energy optical excitation is strongly localized on the metal center, whereas the next optical transition involves the ligand skeleton.

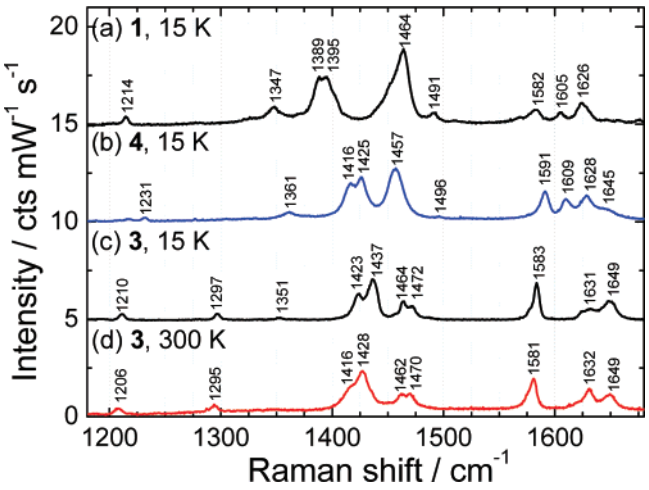

Figure 10. Comparison of the measured Raman spectra of **1** (a), **4** (b), and **3** (c) at 15 K and **3** (d) at 300 K. The spectra were normalized to the intensity of the band at 1395 (a), 1425 (b), 1437 (c), and 1428 cm^{-1} (d).

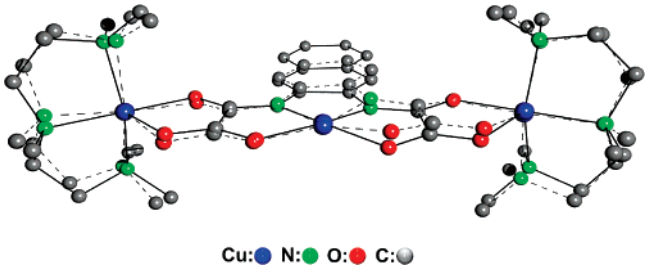

Figure 11. Molecular structures of **3** (dotted line) and **4** (full line), without their weakly coordinating anions and hydrogen atoms (ref 9).

Comparison of Raman Spectra of 1, 3, and 4. The measured Raman spectra of **1**, **3**, and **4** are shown in Figure 10. The spatial extension of the aromatic ring system seems to influence the vibrational properties as reflected by the spectra of **4** (b) and **3** (d) in Figure 10.

A direct comparison of the spectra of **1** (a) and **4** (b) reveals that the coordination of two $[Cu(pmdta)]^{2+}$ on **1** influences mainly the Raman shifts and less the relative intensities since this structural modification keeps roughly the symmetry of the central skeleton. The main differences between the Raman spectra of **1** and **4** arise primarily from the terminal ligands of the coordinated $[Cu(pmdta)]^{2+}$ fragments.

The bands originating from a stretching vibration of CO are shifted to higher frequencies for **4** compared to **1**. Even though the coordination of $[Cu(pmdta)]^{2+}$ changes, the electron density distribution in the central $[Cu(nabo)]^{2-}$ fragment is only marginally affected, and thus the bands of ν(CO) undergo only slight shifts, compare, e.g., 1605 with 1609 cm^{-1} and 1626 with 1628 cm^{-1} for **1** and **4**, respectively. The same is applicable for δ(CH) at 1582 cm^{-1} for **1** and 1591 cm^{-1} for **4**. Much stronger shifts toward higher frequencies appear in the region of CN modes, cf., e.g., 1389 and 1395 cm^{-1} for **1** and 1416 and 1425 cm^{-1} for **4**, respectively.

Even though the Raman-active entity of **1** is two times negatively charged and that of **4** two times positively charged no general tendency of shifting to higher frequencies in the case of **1** compared to **4** was observed, as one might have expected

TABLE 3: *J* Parameters Measured for 3 (a) and 4 (f) and Calculated without Considering the Counterions for 3′ (b and c) and 4′ (g), as Well as Calculated Taking into Consideration the Counterions Coordinating to the Central Cu Atom for 3′ NO_3^- (d and e) and 4′ BF_4^- (h)[a]

	compound	method	J_{12}/cm^{-1}	$J_{12'}/cm^{-1}$	$J_{22'}/cm^{-1}$
(a)	3	measured[b]	-89 ± 2	-89 ± 2	0
(b)	**3′**	calcd, with COSMO	−135	−135	0
(c)	**3′**	calcd, without COSMO	−152	−154	−1
(d)	**3′**NO_3^-	calcd, with COSMO	−134	−136	0
(e)	**3′**NO_3^-	calcd, without COSMO	−215	−210	+26
(f)	**4**	measured[b]	-113 ± 2	-113 ± 2	
(g)	**4′**	calcd, with COSMO	−166	−169	0
(h)	**4′**BF_4^-	calcd, with COSMO	−166	−170	−1
(i)	**4′**BF_4^-	calcd, without COSMO	−244	−260	0

[a] The structural parameters were taken from the X-ray diffraction analysis. [b] Ref 9.

at a first glance. Moreover, a shift in the opposite direction was observed when comparing the band at 1464 for **1** and 1457 cm^{-1} for **4**. One reason may be the coordination of one nitrate counterion on the central Cu(II) ion in the case of **4** which increases the negative charge in this complex.

More obvious is the influence of the size of the aromatic system of the compounds **3** and **4** on their Raman spectra. For example, the rotation vibration of the aromatic CH appears at 1583 cm^{-1} for **3** and 1591 cm^{-1} for **4**. Such differences can be also detected for bands above 1600 cm^{-1}, cf., Figure 10.

All the investigated complexes show similar temperature dependence. An exemplary comparison of the Raman spectra at 15 and 300 K is shown in Figure 9 for complex **3**. For most of the bands only minor changes in the intensity and frequency shifts were observed. Remarkable shifts of 9 cm^{-1} were observed for 1416/1428 cm^{-1} for 300 K and 1425/1437 cm^{-1} for 15 K. These bands were assigned to δ(NCuN, OCuO), ν-(CC) of the aromatic ring and the oxamato group and the δ-(CH) of the aliphatic hydrogens. The shift to higher wavenumbers during decreasing the temperature is caused by decreasing bond lengths in the molecule. The fact that not all bands shift by the same amount indicates that different bonds undergo different length change.

Monitoring the temperature-dependent Raman spectra shows that the above-described changes occur and saturate at temperatures above 100 K. Below 50 K, where the magnetic superexchange overcomes the thermic energy, no more changes were observed in the spectra, clearly indicating that the onset of the magnetic coupling does not imply a significant change in the intramolecular bond angles or bond lengths. The quantum chemical DFT calculations for different spin states will give a rough estimate on the magnitude of such effects, cf., discussions below.

Calculation of Magnetic Superexchange Parameters. Calculated and measured values for magnetic coupling parameters of **3** and **4** are collected in Table 3. Both compounds were treated without the counterion that is weakly coordinating to the central Cu atom, **3′** and **4′**, as well as including the respective ion, **3′**NO_3^- and **4′**BF_4^-. For each case the eigenenergies for the four different magnetic states were calculated using the COSMO model. In addition, calculations without the COSMO model were carried out for **3′** and **3′**NO_3^-. The coupling parameters were obtained by inserting the respective energies into eq 2 and solving this system of equations.

In all cases calculated coupling parameters are significantly larger than the measured ones, which is not untypical. Coupling parameters are usually largely overestimated by pure DFT methods and underestimated by Hartree−Fock. The hybrid functional B3LYP, which contains 20% Hartree−Fock exchange, still tends to overestimate these quantities.[26,27] Moreover, the calculated coupling parameters correspond to energy differences between the magnetic states of ca. 10 meV, which in terms of DFT is very small. The values calculated within the COSMO model are ca. 1.5 times larger than those experimentally determined, independently of whether the counterions are considered or neglected. Without COSMO the differences to the experimental values are larger: for **3′** one obtains a factor of 1.7, whereby the explicit consideration of the counterion leads to even larger discrepancies; the values for **3′**NO_3^- (without COSMO) are more than twice as large as the experimental data. The trends are very similar for **4**, **4′**, and **4′**BF_4^-.

Even though the calculated values for *J* deviate significantly from the experiment, the experimentally observed differences between **3** and **4** are very well reproduced by **3′** and **4′**. According to the experimental results, the coupling parameter J_{12} is larger by 27% for **4** as compared to **3**, whereas the values calculated for **4′** (or **4′**BF_4^-) are larger than those calculated for **3′** (or **3′**NO_3^-) by ca. 25%, when results obtained with the same method are compared. The difference in coupling constants of **3** and **4** thus obviously cannot be traced back to different counterions but rather to the structural differences of the two molecules themselves. On one hand these can be differences in stoichiometry (opba vs nabo), on the other hand different structure parameters due to packing effects can play a role. In order to find out which of these two factors brings the larger contribution, we calculated the coupling parameters of an artificial species, which is of the composition of **3′**, but of the geometric structure of **4′**. This molecule was obtained by removing four C and four H atoms of the terminal phenyl ring in **4′** and adding two H instead without any further structural modifications. For this structure we found (using the COSMO model and neglecting the counterion) $J_{12} = -167$ cm^{-1}, $J_{12'} = -164$ cm^{-1}, and $J_{22'} = 1$ cm^{-1}, which is practically identical with the values obtained for **4′**. Thus we may conclude that the difference in coupling parameters of **3** and **4** mainly arise from differences in the geometric structure due to packing effects. The choice of the counterion (NO_3^- or BF_4^-) or of the organic bridge (opba or nabo) is of much less significant influence. The latter conclusion is further supported by the previous experimental observation[28] that the spin density distribution of the respective mononuclear precursor molecules [Cu(opba)]$(^nBu_4N)_2$ and [Cu(nabo)]$(^nBu_4N)_2$ (**1**) does not significantly vary with replacing the aromatic systems.

Packing effects, which are generally understood as effects caused by the arrangement of molecules to each other in the solid state, lead to different local geometry for the Cu atoms in **3** and **4** and hence to differences in the overlap of magnetic orbitals which is finally reflected in different coupling parameters. The differences between the molecular structures of **3** (dotted line) and **4** (full line) are shown in Figure 11, and a

more detailed structural discussion can be found in ref 9. The coordination environment around the Cu1 is square planar, and the magnetic orbitals are described by $d_{x^2-y^2}$ (taking the Cu−O bonds as *x*- and *y*-axes). The terminal Cu(II) ions are pentacoordinated, which implies an intermediate environment between square planar and trigonal bipyramidal coordination geometry. The molecular structure of **3** is closer to trigonal bipyramidal for which the overlap of the magnetic orbitals is more reduced in comparison to **4** resulting in a weaker magnetic superexchange interaction for **3**.

Summary and Conclusions

This work presents an analysis of the influence of a systematic variation of the molecular structure on the optical, vibrational, and magnetic properties of four Cu(II)−bis(oxamato) complexes. This class of molecules is a highly interesting model system due to its structural flexibility, which allows us to vary the type of the metal atoms, their number, as well as the bridging ligands. This structural flexibility provides the possibility to tune the molecular structure to induce physical properties required by a desired application. For example, the trinuclear complex **3** was the first multimetallic paramagnetic molecule deposited in a controlled way on a surface by means of spin coating and the mononuclear precursor molecules of it were used for the synthesis of single-molecule magnets.

Replacing the metal atom in the mononuclear complexes was found to yield dramatic shifts in the energy of the optical transitions, as shown by UV−vis absorption measurements on solution. On the other hand, the extension of the aromatic system of the bridging ligand brings more influence on the intensity of the CT and $\pi-\pi^*$ optical transitions in the UV range as demonstrated by the optical absorption measurements on the solution as well as by the ellipsometric measurements on the films of the trinuclear complexes **3** and **4**.

A first comprehensive assignment of the vibrational bands of the bis(oxamato) type transition metal complexes is proposed for **1**−**3** by a detailed comparison of the experimental spectra with the vibrational energies as well as IR and Raman intensities calculated using DFT. For example, the replacement of Cu with Ni in the mononuclear complexes was found to induce significant frequency shifts (up to 6 cm^{-1}) of the bands involving vibrations of the coordinating N and O atoms while having less influence on the bands stemming from the terminal ligands. Moreover, temperature-dependent RS investigations show that the onset of superexchange interactions at low temperatures does not involve a modification of the structural parameters. The expected size of this effect was theoretically studied for different spin states.

Furthermore, computational studies using the broken symmetry approach on the magnetic properties of **3** and **4** were performed showing the tremendous influence of packing effects supporting the experimental results reported previously. The influence of different counterions and organic N,N′-bridges, on the other hand, is much less important.

Acknowledgment. B. Bräuer thanks the Fonds der Chemischen Industrie and the Marie Curie program for two Ph.D. fellowships.

Supporting Information Available: ψ and Δ ellipsometric parameters of **4** as determined experimentally with the corresponding fitting curves, the real part of the dielectric function ϵ_1 of **3** and **4**, the Raman spectra of **4** of a powder sample and a spin-coated thin film, and Ortep plots of **3′**NO_3^- and **4′**BF_4^-. This material is available free of charge via the Internet at http://pubs.acs.org.

References and Notes

(1) Naber, W. J. M.; Faez, S.; Wiel, W. G. *J. Phys. D: Appl. Phys.* **2007**, *40*, R205.
(2) Miller, J. S.; Epstein, A. J. *MRS Bull.* **2000**, *25*, 21.
(3) Kahn, O. *Molecular Magnetism*; VCH: Weinheim, Germany, 1993.
(4) Costa, R.; Garcia, A.; Ribas, J.; Mallah, T.; Journaux, Y. *Inorg. Chem.* **1993**, *32*, 3733.
(5) Stumpf, H. O.; Ouahab, L.; Pei, Y.; Grandjean, D.; Kahn, O. *Science* **1993**, *261*, 447.
(6) Dias, A. C.; Knobel, M.; Stumpf, H. O. *J. Magn. Magn. Mater.* **2001**, *226*, 1961.
(7) Pereira, C. L. M.; Pedroso, E. F.; Novak, M. A.; Brandl, A. L.; Knobel, M.; Stumpf, H. O. *Polyhedron* **2003**, *22*, 2387.
(8) Costa, R.; Garcia, A.; Sanchez, R.; Ribas, J.; Solans, X.; Rodriguez, V. *Polyhedron* **1993**, *12*, 2697.
(9) Rüffer, T.; Bräuer, B.; Powell, A.; Hewitt, I.; Salvan, G. *Inorg. Chim. Acta* **2007**, *360* (11), 3475.
(10) Bräuer, B.; Rüffer, T.; Kirmse, R.; Griebel, J.; Weigend, F.; Salvan, G. *Polyhedron* **2007**, *26*, 1773.
(11) Bräuer, B.; Zahn, D. R. T.; Rüffer, T.; Salvan, G. *Chem. Phys. Lett.* **2006**, *432*, 226.
(12) Cervera, B.; Sanz, J. L.; Ibanez, M. J.; Vila, G.; Lloret, F.; Julve, M.; Ruiz, R.; Ottenwaelder, X.; Aukauloo, A.; Poussereau, S.; Yournaux, Y.; Munoz, M. C. *J. Chem. Soc., Dalton Trans.* **1998**, 781.
(13) Lee, C.; Yang, W.; Parr, R. G. *Phys. Rev. B* **1988**, *37*, 785.
(14) (a) Becke, A. D. *Phys. Rev. A: At., Mol., Opt. Phys.* **1988**, *38*, 3098. (b) Becke, A. D. *J. Chem. Phys.* **1993**, *98*, 1372. (c) Becke, A. D. *J. Chem. Phys.* **1993**, *98*, 5648.
(15) Frisch, M. J.; Trucks, G. W.; Schlegel, H. B.; Scuseria, G. E.; Robb, M. A.; Cheeseman, J. R.; Montgomery, J. A., Jr.; Vreven, T.; Kudin, K. N.; Burant, J. C.; Millam, J. M.; Iyengar, S. S.; Tomasi, J.; Barone, V.; Mennucci, B.; Cossi, M.; Scalmani, G.; Rega, N.; Petersson, G. A.; Nakatsuji, H.; Hada, M.; Ehara, M.; Toyota, K.; Fukuda, R.; Hasegawa, J.; Ishida, M.; Nakajima, T.; Honda, Y.; Kitao, O.; Nakai, H.; Klene, M.; Li, X.; Knox, J. E.; Hratchian, H. P.; Cross, J. B.; Bakken, V.; Adamo, C.; Jaramillo, J.; Gomperts, R.; Stratmann, R. E.; Yazyev, O.; Austin, A. J.; Cammi, R.; Pomelli, C.; Ochterski, J. W.; Ayala, P. Y.; Morokuma, K.; Voth, G. A.; Salvador, P.; Dannenberg, J. J.; Zakrzewski, V. G.; Dapprich, S.; Daniels, A. D.; Strain, M. C.; Farkas, O.; Malick, D. K.; Rabuck, A. D.; Raghavachari, K.; Foresman, J. B.; Ortiz, J. V.; Cui, Q.; Baboul, A. G.; Clifford, S.; Cioslowski, J.; Stefanov, B. B.; Liu, G.; Liashenko, A.; Piskorz, P.; Komaromi, I.; Martin, R. L.; Fox, D. J.; Keith, T.; Al-Laham, M. A.; Peng, C. Y.; Nanayakkara, A.; Challacombe, M.; Gill, P. M. W.; Johnson, B.; Chen, W.; Wong, M. W.; Gonzalez, C.; Pople, J. A. *Gaussian 03*, revision C.02; Gaussian, Inc.: Wallingford, CT, 2004.
(16) (a) *TURBOMOLE* V5−8; University of Karlsruhe. (b) Horn, H.; Weiss, H.; Häser, M.; Ehrig, M.; Ahlrichs, R. *J. Comput. Chem.* **1991**, *12*, 1058. (c) Häser, M.; Ahlrichs, R.; Baron, H. P.; Weis, P.; Horn, H. *Theor. Chim. Acta* **1992**, *83*, 455. (d) Schäfer, A.; Horn, H.; Ahlrichs, R. *J. Chem. Phys.* **1992**, *97*, 2571. (e) Schäfer, A.; Huber, C.; Ahlrichs, R. *J. Chem. Phys.* **1994**, *100*, 5829. (f) Ahlrichs, R.; Bär, M.; Häser, M.; Horn, H.; Kölmel, C. *Chem. Phys. Lett.* **1989**, *162*, 165.
(17) Eichkorn, K.; Treutler, O.; Öhm, H.; Häser, M.; Ahlrichs, R. *Chem. Phys. Lett.* **1995**, *240*, 283.
(18) Weigend, F.; Ahlrichs, R. *Phys. Chem. Chem. Phys.* **2005**, *7*, 3297.
(19) Weigend, F. *Phys. Chem. Chem. Phys.* **2006**, *8*, 1057.
(20) Klamt, A.; Schürmann, G. *J. Chem. Soc., Perkin Trans. 2* **1993**, 799.
(21) Noodleman, L.; Norman, J. G. *J. Chem. Phys.* **1979**, *70*, 4903.
(22) Noodleman, L. *J. Chem. Phys.* **1981**, *74*, 5737.
(23) (a) Bencini, A.; Totti, F. *Int. J. Quantum Chem.* **2005**, *101*, 819. (b) Adamo, C.; Barone, V.; Bencini, A.; Totti, F.; Ciofini, I. *Inorg. Chem.* **1999**, *38*, 1996.
(24) Arbuznikov, A. V.; Kaupp, M.; Malkin, V. G.; Reviakine, R.; Malkina, O. L. *Phys. Chem. Chem. Phys.* **2002**, *4*, 5467.
(25) Ong, K. K.; Jensen, J. O.; Hameka, H. F. *J. Mol. Struct. (THEOCHEM)* **1999**, *459*, 131.
(26) Sun, Y.; Liu, C.; Qi, Z.; Zhang, D. *J. Mol. Struct. (THEOCHEM)* **2005**, *718*, 49.
(27) Ruiz, E.; Rodríguez-Fortea, A.; Tercero, J.; Cauchy, T.; Massobrio, C. *J. Chem. Phys.* **2005**, *123*, 074102.
(28) Bräuer, B.; Weigend, F.; Fittipaldi, M.; Gatteschi, D.; Reijerse, E. J.; Guerri, A.; Ciattini, S.; Salvan, G.; Rüffer, T. Submitted for publication.